ADVANCES IN ATMOSPHERIC SCIENCES, VOL. 36, APRIL 2019, 451–464

• **Original Paper** •

Surface Rainfall Processes during the Genesis Period of Tropical Cyclone Durian (2001)

Yaping WANG[1,3], Yongjie HUANG[1,3], and Xiaopeng CUI*[1,2,3]

[1] *Key Laboratory of Cloud-Precipitation Physics and Severe Storms (LACS), Institute of Atmospheric Physics, Chinese Academy of Sciences, Beijing* 100029*, China*

[2] *Collaborative Innovation Center on Forecast and Evaluation of Meteorological Disasters, Nanjing University of Information Science and Technology, Nanjing* 210044*, China*

[3] *University of Chinese Academy of Sciences, Beijing* 100049*, China*

(Received 24 July 2018; revised 4 September 2018; accepted 29 November 2018)

ABSTRACT

The rainfall processes during the formation of tropical cyclone (TC) Durian (2001) were investigated quantitatively using the three-dimensional (3D) WRF-based precipitation equation. The rain rate (P_S) decreased slightly as the TC approached to formation, and then increased as Durian began to intensify. The rate of moisture-related processes (Q_{WV}) in the equation contributed around 80% to P_S before TC genesis, and made more contribution during and after TC genesis. The rate of hydrometeor-related processes (Q_{CM}) contributed about 20% before TC formation, followed by less contribution during and after TC formation. Q_{WV} were dominated by the 3D moisture flux advection rate (Q_{WVA}), while the surface evaporation rate (Q_{WVE}) also played an important role. Just before TC genesis, moisture from Q_{WVA} and Q_{WVE} helped the local atmosphere moisten (negative Q_{WVL}). Q_{CM} were determined by the 3D hydrometeor advection rates (Q_{CLA} and Q_{CIA}) and the local change rates of hydrometeors (Q_{CLL} and Q_{CIL}). During TC formation, Q_{CM} largely decreased and then reactivated as Durian began to intensify, accompanied by the development of TC cloud. Both the height and the strength of the net latent heating center associated with microphysical processes generally lowered before and during TC genesis, resulting mainly from lessening deposition and condensation. The downward shift of the net latent heating center induced a more bottom-heavy upward mass flux profile, suggesting to promote lower-tropospheric convergence in a shallower layer, vorticity amplification and TC spin-up.

Key words: surface rainfall processes, tropical cyclone formation, three-dimensional precipitation equation, latent heating

Citation: Wang, Y. P., Y. J. Huang, and X. P. Cui, 2019: Surface rainfall processes during the genesis period of tropical cyclone Durian (2001). *Adv. Atmos. Sci.*, **36**(4), 451–464, https://doi.org/10.1007/s00376-018-8157-8.

Article Highlights:

- The rainfall processes during tropical cyclone (TC) formation were investigated quantitatively using the 3D precipitation equation.
- The moisture-related processes contributed more than 80% to the rainfall while the hydrometeor-related processes contributed about 20%.
- The net latent heating profile associated with the cloud microphysics changed, inducing more bottom-heavy upward mass flux.

1. Introduction

Precipitation is not only associated with water vapor supply and cloud microphysical processes, but also impacted by dynamic and thermodynamic conditions (Liao et al., 2006). In fact, surface rainfall processes consist of two parts: (1) the transportation and convergence of water vapor and hydrometeors to the precipitation area under various dynamic and thermodynamic conditions; and (2) the microphysical conversions between water vapor and hydrometeors, as well as between different hydrometeors, followed by precipitation particles falling to the surface (Cui, 2009). The two parts are not independent but interact intricately with each other. Both the water vapor budget and hydrometeor budget are closely related with the precipitation or water budget in the atmosphere. Gao et al. (2005) derived a surface rainfall equation, which connected the water vapor budget

* Corresponding author: Xiaopeng CUI
E-mail: xpcui@mail.iap.ac.cn

and hydrometeor budget with the surface rain rate (P_S) in a two-dimensional (2D) cloud-resolving model (CRM) framework. This 2D CRM-based surface rainfall equation has been widely used in quantitative analysis of tropical rainfall processes (Cui and Li, 2006, 2009, 2011; Li, 2006; Cui et al., 2007; Ping et al., 2007, 2008; Wang et al., 2007; Xu et al., 2007; Cui, 2008, 2009; Gao et al., 2009; Yue et al., 2009; Gao and Li, 2010; Li et al., 2011; Shen et al., 2011a, b, c; Li and Gao, 2016), as well as rainfall processes associated with landfalls of tropical cyclones (TCs) (Cui and Xu, 2009; Wang et al., 2009, 2010a; Yue et al., 2009; Yue and Shou, 2011). The 2D CRM in the aforementioned studies is forced to integrate by imposing zonally uniform vertical velocity, zonal wind and so on (Wang et al., 2010a; Li and Gao, 2016). Based on Gao et al. (2005), Huang et al. (2016) further developed a precipitation equation in the three-dimensional (3D) Weather Research and Forecasting (WRF) model framework. This 3D WRF-based precipitation equation has been applied to investigate the torrential rainfall processes in Sichuan Province, China (Huang et al., 2016), as well as the rainfall processes in a landed TC (Liu and Cui, 2018) and the rainfall processes associated with a TC over ocean (Wang et al., 2018b). Similar 3D water budget methods have also been applied in several TC precipitation studies. Braun (2006) found that most condensation in the eyewall occurs in convective hot towers, while outside of the eyewall stratiform precipitation processes play a larger role. Yang et al. (2011) used the water budget to diagnose the precipitation associated with TC Nari (2001) over the ocean, pointing out that the horizontal water vapor convergence accounted for 88% of the net condensation. Both Braun (2006) and Yang et al. (2011) suggested that the ocean source of water vapor in the inner core is a small portion. Huang et al. (2014) showed that water vapor condensation and raindrop evaporation in the torrential rainfall associated with Typhoon Morakot (2009) were strongly influenced by orographic uplift. Xu et al. (2017) utilized the water budget to investigate the torrential rainfall associated with Typhoon Fitow (2014) over coastal areas and suggested that the rainfall centers were associated with water vapor convergence, condensation, accretion of cloud water by raindrops, and raindrop loss/convergence. Although the above 2D and 3D precipitation equations have already been used to investigate the rainfall processes associated with TCs (Cui and Xu, 2009; Wang et al., 2009, 2010a, 2018b; Yue et al., 2009; Yue and Shou, 2011; Liu and Cui, 2018), the rainfall processes during TC genesis have seldom been studied with the equation.

Precipitation evolution during TC formation has recently begun to receive more attention in the literature. Wang and Hankes (2016) analyzed composites of precipitation and column water vapor retrieved from the SSM/I and SSMIS passive microwave instruments during TC formation. It was found that precipitation is weak and scattered in the radial direction prior to 48 hours before formation, followed by high column water vapor near the pouch center increasing prior to genesis, then precipitation increasing substantially and distributing more symmetrically, as a result of deep convection bursting in the pouch center. Moreover, latent heat releases of cloud microphysical processes associated with precipitation, such as water vapor condensation and deposition, are important for driving the transverse circulation and strengthening the low-level circulation in TC formation (Montgomery et al., 2006; Wang et al., 2010b). The intensification of the secondary circulation is attributed to the concentrated latent heating induced by the organized convection and the associated low-level inflow moisture convergences at large radii, fueling further precipitation in turn (Fritz and Wang, 2014). From the energy budget perspective, Wang et al. (2016a) suggested that the latent heat released by moist convection accumulates and transforms into potential energy, and eventually converts to the horizontal kinetic energy of the near-surface circulation, indicating the spin-up of the TC vortex. Raymond et al. (2011) and Raymond (2012) also found that increased stabilization of the atmosphere, as a result of latent heating in the middle troposphere and latent cooling in the lower troposphere, is conducive to the transition of the upward mass flux profile from top-heavy to bottom-heavy. As a result, the increasing vertical gradient of vertical mass flux induces convergence of mass and vorticity at a shallow layer in the lower troposphere, leading to the spin-up of a vortex near the surface.

During TC genesis, the water vapor content and cloud structures are closely related to dynamic and thermodynamic conditions of atmosphere. In this study, the 3D WRF-based precipitation equation (Huang et al., 2016) is for the first time applied in TC genesis, in which the contributions of moisture-related processes and hydrometeor-related processes to the precipitation during the formation of TC Durian (2001) are quantitatively diagnosed based on high-resolution simulation data (Wang et al., 2016b). The roles of cloud microphysical processes and their associated latent heating in TC formation will also be investigated. This study could give some hints on how moisture and cloud hydrometeors, as well as precipitation evolution, affect the establishment of the near-surface vortex in TC genesis.

The paper is organized as follows. Section 2 briefly describes the 3D WRF-based precipitation equation. Section 3 presents the rainfall processes, including water vapor–related processes and hydrometeor-related processes associated with the formation of TC Durian. Section 4 emphasizes the microphysical conversion processes and their related latent heat releases during TC formation in more detail, as well as their role in the TC vortex spin-up. A summary and conclusions are provided in section 5.

2. The 3D WRF-based precipitation equation

Based on the water budget balance in the atmosphere, Gao et al. (2005) derived a surface precipitation equation by combining the water vapor budget and the hydrometeor budget in a 2D CRM framework, which was further extended by Huang et al. (2016) in the 3D WRF model framework:

$$P_S = Q_{WV} + Q_{CM} . \quad (1)$$

Equation (1) is derived based on the governing equations for water species in the WRF model (Skamarock et al., 2008):

$$\frac{\partial(\rho_a Q_v)}{\partial t} = \mathrm{ADV}_{Q_v} + \mathrm{DIFF}_{Q_v} + E_s + \rho_a S_{Q_v}; \quad (2)$$

$$\frac{\partial(\rho_a Q_c)}{\partial t} = \mathrm{ADV}_{Q_c} + \mathrm{DIFF}_{Q_c} + \rho_a S_{Q_c}; \quad (3)$$

$$\frac{\partial(\rho_a Q_x)}{\partial t} = \mathrm{ADV}_{Q_x} + \mathrm{DIFF}_{Q_x} + \mathrm{SEDI}_{Q_x} + \rho_a S_{Q_x}, x \in (r,i,s,g,h)\,. \quad (4)$$

Here, Q_v, Q_c, and Q_x are the mixing ratios of water species (v: water vapor; c: cloud water; r: rain water; i: cloud ice; s: snow; g: graupel; h: hail); terms $\mathrm{ADV}_{Q_v} = -\nabla_3 \cdot (\rho_a Q_v \boldsymbol{V})$, $\mathrm{ADV}_{Q_c} = -\nabla_3 \cdot (\rho_a Q_c \boldsymbol{V})$, and $\mathrm{ADV}_{Q_x} = -\nabla_3 \cdot (\rho_a Q_x \boldsymbol{V})$ are 3D advection terms or 3D flux convergence/divergence terms; terms DIFF_{Q_v}, DIFF_{Q_c} and DIFF_{Q_x} are diffusion terms; E_s is the surface moisture flux; SEDI_{Q_x} is the sedimentation term; ρ_a is the air density; $\boldsymbol{V}$ is the three-dimensional wind vector; and S_{Q_v}, S_{Q_c} and S_{Q_x} are source/sink terms associated with cloud microphysical processes. A 3D WRF-based precipitation equation was derived from the above equations, Eqs. (2)–(4), by combination and vertical integrations (Huang et al., 2016):

$$\begin{aligned}
\int_{z_b}^{z_t}\left(\sum_{x\in(r,i,s,g,h)} -\mathrm{SEDI}_{Q_x}\right)dz = {} & \int_{z_b}^{z_t}\left(-\sum\frac{\partial \rho_a Q_v}{\partial t}\right)dz + \int_{z_b}^{z_t}\sum \mathrm{ADV}_{Q_v}dz + \int_{z_b}^{z_t}\sum \mathrm{DIFF}_{Q_v}dz + \int_{z_b}^{z_t}\sum E_s dz + \\
P_S \qquad & Q_{WVL} \qquad\qquad Q_{WVA} \qquad\qquad Q_{WVD} \qquad\qquad Q_{WVE} \\
& \int_{z_b}^{z_t}\left(-\sum_{x\in(c,r)}\frac{\partial \rho_a Q_x}{\partial t}\right)dz + \int_{z_b}^{z_t}\sum_{x\in(c,r)} \mathrm{ADV}_{Q_x}dz + \int_{z_b}^{z_t}\sum_{x\in(c,r)} \mathrm{DIFF}_{Q_x}dz + \\
& Q_{CLL} \qquad\qquad Q_{CLA} \qquad\qquad Q_{CLD} \\
& \int_{z_b}^{z_t}\left(-\sum_{x\in(i,s,g,h)}\frac{\partial \rho_a Q_x}{\partial t}\right)dz + \int_{z_b}^{z_t}\sum_{x\in(i,s,g,h)} \mathrm{ADV}_{Q_x}dz + \int_{z_b}^{z_t}\sum_{x\in(i,s,g,h)} \mathrm{DIFF}_{Q_x}dz. \quad (5) \\
& Q_{CIL} \qquad\qquad Q_{CIA} \qquad\qquad Q_{CID}
\end{aligned}$$

Here, z_t and z_b are the top and surface of the model atmosphere, respectively. Note that Q_{WVL}, Q_{CLL} and Q_{CIL} are actually the negative values of vertically integrated $\partial(\rho_a Q_v)/\partial t$, $\partial(\rho_a Q_x)/\partial t[x \in (c,r)]$, and $\partial(\rho_a Q_x)/\partial t[x \in (i,s,g,h)]$, respectively. The surface precipitation rate (P_S) is associated with both water vapor–related processes (Q_{WV}) and hydrometeor-related processes (Q_{CM}). The two kinds of processes are not independent but interact intricately with each other, together determining the rain rate. Q_{WV} include four components: the water vapor local change rate (Q_{WVL}), 3D moisture flux convergence/divergence rate (Q_{WVA}), 3D water vapor diffusion rate (Q_{WVD}), and surface evaporation rate (Q_{WVE}). Q_{CM} include liquid-phase and ice-phase hydrometeor-related processes: the local change rate of liquid-phase hydrometeors (cloud water and rain water) (Q_{CLL}), 3D liquid-phase hydrometeor flux convergence/divergence rate (Q_{CLA}), 3D diffusion rate of liquid-phase hydrometeors (Q_{CLD}), local change rate of ice-phase hydrometeors (cloud ice, snow, graupel and hail) (Q_{CIL}), 3D ice-phase hydrometeor flux convergence/divergence rate (Q_{CIA}), and 3D diffusion rate of ice-phase hydrometeors (Q_{CID}) (Table 1). They are expressed as follows:

$$Q_{WV} = Q_{WVL} + Q_{WVA} + Q_{WVD} + Q_{WVE}; \quad (6)$$

$$Q_{CM} = Q_{CLL} + Q_{CLA} + Q_{CLD} + Q_{CIL} + Q_{CIA} + Q_{CID}\,. \quad (7)$$

The meanings of each term and their sub-terms in Eqs. (1), (6) and (7) are presented in Table 1.

Table 1. Terms in the 3D WRF-based surface precipitation equation.

Term	Description
P_S	Surface precipitation rate
Q_{WV}	Water vapor process
Q_{CM}	Cloud hydrometeors process
Q_{WVL}	Vertically integrated negative local change rate of water vapor (local drying or moistening)
Q_{WVA}	Vertically integrated 3D flux convergence/divergence rate of water vapor
Q_{WVD}	Vertically integrated 3D diffusion rate of water vapor
Q_{WVE}	Surface evaporation rate
Q_{CLL}	Vertically integrated negative local change rate of liquid-phase hydrometeors (cloud water and rain water)
Q_{CLA}	Vertically integrated 3D flux convergence/divergence rate of liquid-phase hydrometeors (cloud water and rain water)
Q_{CLD}	Vertically integrated 3D diffusion rate of liquid-phase hydrometeors (cloud water and rain water)
Q_{CIL}	Vertically integrated negative local change rate of ice-phase hydrometeors (cloud ice, snow, graupel and hail)
Q_{CIA}	Vertically integrated 3D flux convergence/divergence rate of ice-phase hydrometeor (cloud ice, snow, graupel and hail)
Q_{CID}	Vertically integrated 3D diffusion rate of ice-phase hydrometeors (cloud ice, snow, graupel and hail)

3. Surface rainfall processes during TC Durian's genesis

3.1. *Model configuration and precipitation evolution*

The formation process of TC Durian (2001) in the South China Sea (SCS) was successfully simulated by the WRF model with four nesting domains, the resolutions of which were 54, 18, 6, and 1.2 km, respectively (Wang et al., 2016b). The 54-km and 18-km domains integrated for 84 hours, starting at 0000 UTC 28 June and ending at 1200 UTC 1 July 2001, driven by NCEP reanalysis data on $2.5^\circ \times 2.5^\circ$ grids. The 6-km and 1.2-km domains started at 1200 UTC 28 June, 12 hours later than the outer two domains, for the purpose of saving computer resources and allowing the environment to develop in the outer domains. The Goddard microphysics scheme (Tao et al., 1989) and Yonsei University boundary layer scheme (Hong et al., 2006) were used in each domain, while the Kain–Fritsch cumulus parameterization scheme (Kain, 2004) was only used in the outermost two domains. The simulated Durian generated near (16°N, 116.2°E) (about 80 km from the best track data) at about 0800 UTC 29 June 2001, which was just two hours later than observed.

The 6-h accumulated precipitation amounts derived from passive microwave satellite measurements via the Climate Prediction Center morphing technique (CMORPH; Joyce et al., 2004) (Figs. 1a, c, e and g) and simulated by the WRF model (Figs. 1b, d, f and h) are shown in Fig. 1. From 1800 UTC 28 to 0000 UTC 29 June 2001, the satellite-estimated northwest–southeast-oriented rainband associated with a mesoscale convective system (MCS) before Durian's genesis (Fig. 1a) was reproduced fairly well by the model (Fig. 1b). The difference between the satellite-estimated and simulated precipitation intensities may be mainly due to the underestimation of TC rainfall intensities by the satellite (Sapiano and Arkin, 2009; Yu et al., 2009; Pan et al., 2011; Chen et al., 2015), as well as the relatively coarser horizontal resolution of the satellite estimation (8 km) than the simulation (1.2 km). From 0000 to 0600 UTC 29 June 2001, the satellite-estimated precipitation center near (14°N, 116°E) (Fig. 1c) gradually separated from the MCS rain belt and later developed into the TC-associated precipitation (Figs. 1e and g). Meanwhile, the simulated scattering precipitation (Fig. 1b) to the north of the MCS gradually developed and intensified with cyclonic distribution, and at the same time the rainband associated with the MCS was gradually narrowing and weakening (Figs. 1d, f and h). Overall, despite some differences between the satellite-estimated and the simulated precipitation, the WRF model basically reproduced the evolution characteristics of rainfall associated with the MCS, as well as the TC spin-up.

The time series of the satellite-estimated and simulated rain rates averaged in a 240 km-radius circular domain are presented in Fig. 2. The centers of the circular domains were selected as the centers of a midlevel mesoscale convective vortex (MCV) before Durian's formation and the TC centers after its genesis, moving with time (Wang et al., 2016b). The midlevel MCV formed a favorable area for TC genesis, just like the pouch areas described in Dunkerton et al. (2009) and Wang et al. (2010b). The satellite-estimated rain rate was much smaller than the simulated one before 2300 UTC 28 June 2001, but after that the simulated rain rate followed the satellite-estimated one reasonably well. The difference in rain rates was due to the differences in rainfall distributions and intensities between the satellite estimation and simulation. With the formation of TC Durian (0200–1400 UTC 29 June 2001), both the satellite-estimated and simulated rain rates gradually decreased, and then increased as Durian began to intensify after 1400 UTC 29 June 2001.

3.2. *Surface rainfall processes during TC Durian's genesis*

The time series of area-averaged (in the 240 km-radius circular domain) terms in the 3D WRF-based precipitation equation [Eqs. (1), (6) and (7), Table 1] from 1400 UTC 28 to 2000 UTC 29 June 2001 are shown in Fig. 3. Q_{WV} was the major contributor to the P_{S} (Fig. 3a), accounting for more than 70% of it (Fig. 3b). Before Durian's genesis, the ratio of Q_{WV} to P_{S} was relatively small (around 80%), and the ratio increased distinctly during and after Durian's formation (Fig. 3b). Q_{CM} accounted for around 20% of the P_{S} before TC genesis, and the ratio of Q_{CM} to P_{S} decreased quickly during genesis, followed by reactivation as Durian began to intensify (Fig. 3).

According to Eq. (6), Q_{WV} consists of four parts: Q_{WVL}, Q_{WVA}, Q_{WVE} and Q_{WVD} (Fig. 4a). Q_{WVA} presented similar magnitude and evolution as Q_{WV} (Fig. 4a). Moisture flux convergence ($Q_{\mathrm{WVA}} > 0$) dominated the water vapor budget (Q_{WV}) over the ocean, with distinct "lower-tropospheric convergence superposed with upper-level divergence" structure (Fig. 5b) and upward vertical mass flux (Fig. 5a). Before Durian's genesis (1400 UTC 28 to 0200 UTC 29 June 2001), a mature MCS existed (Fig. 1b), with a thicker convergence level (Fig. 5b) and higher upward vertical mass flux center (Fig. 5a). Besides, a positive relative vorticity center existed in the mid-troposphere, with a maximum value located at around 4 km (Fig. 5c). Zhang et al. (2008) and Wang et al. (2016b) suggested that the midlevel cyclonic relative vorticity could be attributed to the development of a mid-level MCV on the north side of the MCS, which formed a favorable environment for Durian's genesis. The thicker lower-tropospheric convergence level (Fig. 5b) and higher upward vertical mass flux center (Fig. 5a) before Durian's genesis were mainly caused by the MCS. The MCS gradually moved out of the 240 km-radius circular domain during 2200 UTC 28 June to 0200 UTC 29 June. Thus, the upward vertical mass flux (Fig. 5a), the low-level convergence (Fig. 5b) and Q_{WVA} (Fig. 4a) slightly decreased. From 0200 to 0800 UTC 29 June 2001, convection gradually organized in the strengthening MCV (Wang et al., 2016b) (Fig. 1d), producing a vertical upward mass flux center at about $z = 5$ km (Fig. 5a) and distinct lower-tropospheric convergence (Fig. 5b). Meanwhile, the positive relative vorticity center moved from around 4 km to ~ 1.5 km (Fig. 5c), suggesting gradual establishment of the lower-tropospheric TC vortex (Fig. 1d). After Durian's genesis at

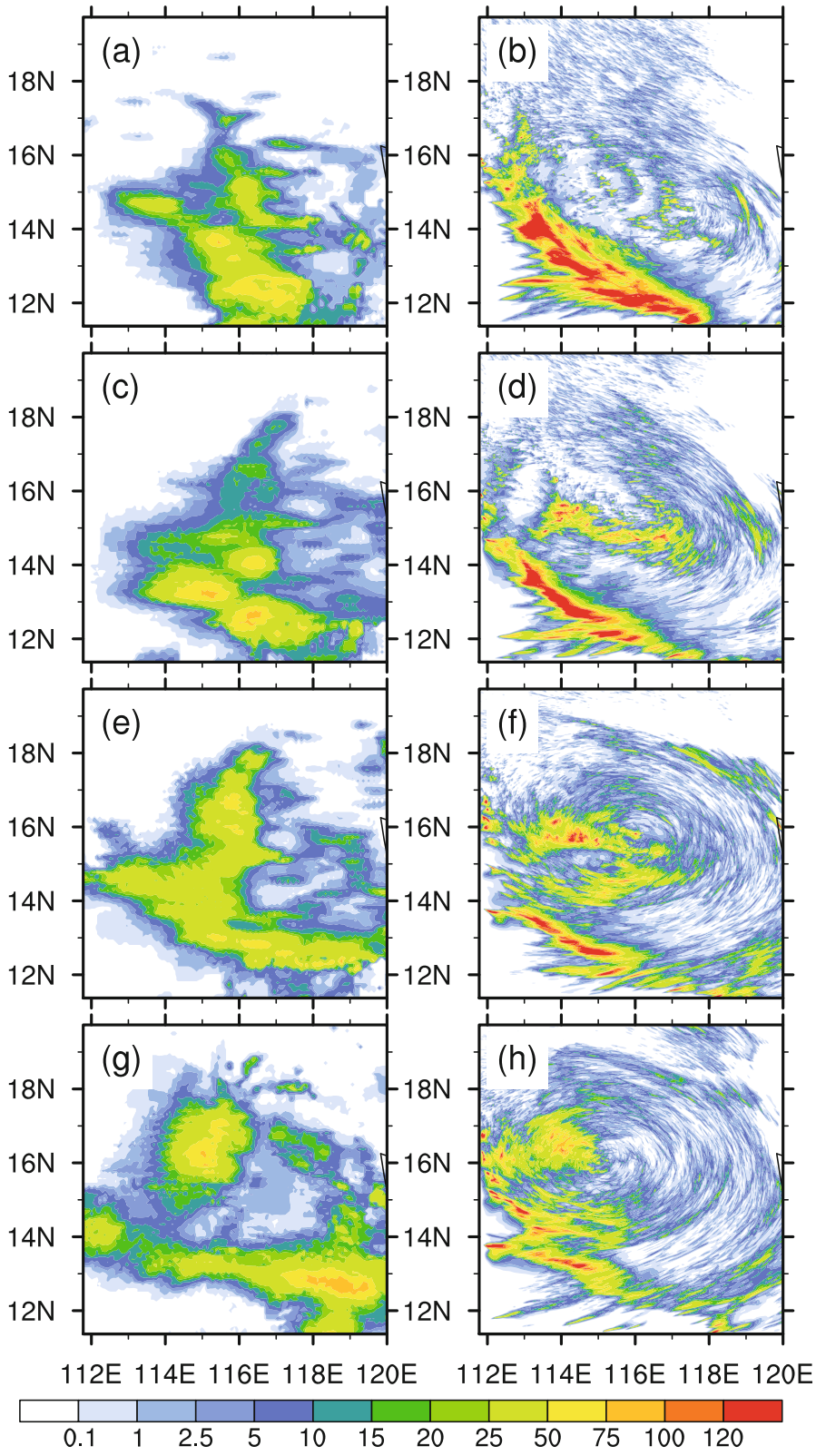

Fig. 1. Six-hour accumulated precipitation (units: mm) retrieved from (a, c, e, g) satellite measurements via the CMORPH technique with a horizontal resolution of 8 km, and (b, d, f, h) the model with a horizontal resolution of 1.2 km: (a, b) 1800 UTC 28 June to 0000 UTC 29 June; (c, d) 0000 UTC to 0600 UTC 29 June; (e, f) 0600 UTC to 1200 UTC 29 June; (g, h) 1200 UTC to 1800 UTC 29 June.

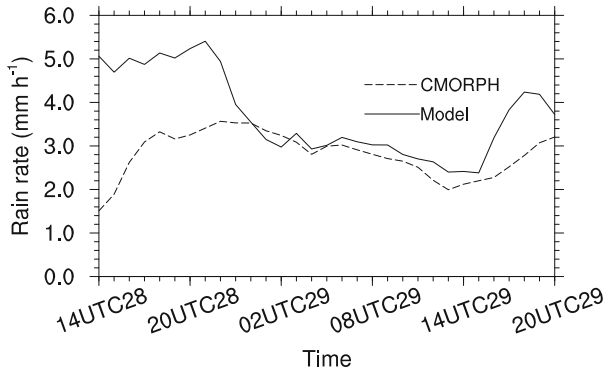

Fig. 2. Time series of area-averaged precipitation from CMORPH satellite data (dashed line) and from the model simulation (solid line) in a 240-km-radius area (units: mm h^{-1}) from 1400 UTC 28 June to 2000 UTC 29 June 2001.

0800 UTC 29 June 2001, with gradual intensification of the TC vortex, positive vorticity amplified (Fig. 5c). Meanwhile, the vertical upward mass flux (Fig. 5a), the low-level convergence (Fig. 5b) and Q_{WVA} (Fig. 4a) also intensified. Apart from the dominant role of Q_{WVA} in Q_{WV} (Fig. 4a), Q_{WVE} also made an indispensable positive contribution to Q_{WV}. Considering the surface evaporation outside the 240 km-radius circular domain, which could be further transported (Q_{WVA}) into the circular domain, the contribution of surface evaporation from the ocean to Q_{WV} should be bigger. Q_{WVL} was generally small during the analysis period (Fig. 4a), while just before Durian's genesis (From 0200 to 0800 UTC 29 June 2001) Q_{WVL} presented distinct negative values (Fig. 4a), which suggested the local atmospheric volume (in the 240 km-radius circular domain) was moistening due to sufficient water vapor supply.

The rate of hydrometeor-related processes (Q_{CM}) includes two parts: rates of liquid-phase and ice-phase hydrometeor-related processes [Eq. (7)]. Liquid-phase hydrometeors consist of cloud water and rain water, while ice-phase hydrometeors consist of cloud ice, snow and graupel in this study. The rates of each term [Eq. (7) and Table 1] during the analysis period are presented in Figs. 4b and c. The 3D flux convergence/divergence rates (Q_{CLA}, Q_{CIA}) and the local change rates (Q_{CLL}, Q_{CIL}) of hydrometeors were the dominant terms in both liquid-phase and ice-phase hydrometeor-related rates (Figs. 4b and c). Before Durian's formation at 0800 UTC 29 June, Q_{CLA} and Q_{CIA} both made a positive contribution to Q_{CM}, especially Q_{CIA}. Positive Q_{CLA} and Q_{CIA} suggested that there were hydrometeors aggregating into the 240 km-radius circular volume. From 0400 to 1400 UTC 29 June, both Q_{CLA} and Q_{CIA} decreased to about zero, but with small positive Q_{CLA} and negative Q_{CIA} due to the vertical dynamical structure (Fig. 5b). This will be analyzed in detail later. After 1400 UTC 29 June, both positive Q_{CLA} and negative Q_{CIA} increased slightly due to the intensified "lower-tropospheric convergence superposed with upper-level divergence" dynamical structure (Fig. 5b) during Durian's intensification. The variations of local change rates of hydrometeors (Q_{CLL}, Q_{CIL}) were mainly caused by the 3D flux convergence/divergence rates of hydrometeors (Q_{CLA}, Q_{CIA}), the microphysical conversion rates, as well as the P_S [Eqs. (3) and (4)]. Before 0000 UTC 29 June, both Q_{CLL} and Q_{CIL} were positive, suggesting a continuous decrease in hydrometeors in the MCS (Fig. 1) to feed the rainfall. From 0000 to 0800 UTC 29 June, with the decreasing P_S (Fig. 3a), aggregation of hydrometeors by flux convergence (Figs. 4b, c), and cloud system spin-up (Fig. 1) due to microphysical processes, both Q_{CLL} and Q_{CIL} became negative, suggesting the development of TC-related cloud hydrometeors. After 0800 UTC 29 June, short-term small and positive Q_{CLL} and Q_{CIL} may have been mainly caused by consumption due to rainfall (Fig. 3a) under a relatively weak "lower-tropospheric convergence superposed with upper-level divergence" dynamical structure (Fig. 5b). Later, with the re-strengthening vertical "lower-tropospheric convergence superposed with upper-level divergence" dynamical structure (Fig. 5b), hydrometeors in the 240 km-radius circular volume increased distinctly

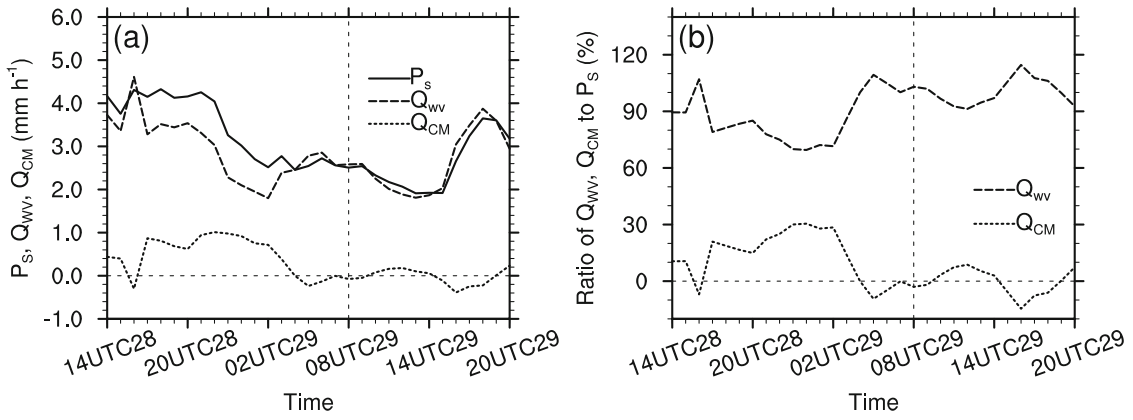

Fig. 3. Time series of (a) area-averaged surface rain rate (P_S, solid line), moisture-related processes (Q_{WV}, long dashed line), and cloud-related processes (Q_{CM}, short dashed line) (units: mm h^{-1}), and (b) the ratios (units: %) of Q_{WV} (long dashed line) and Q_{CM} (short dashed line) to P_S from 1400 UTC 28 June to 2000 UTC 29 June 2001 in a 240-km-radius domain.

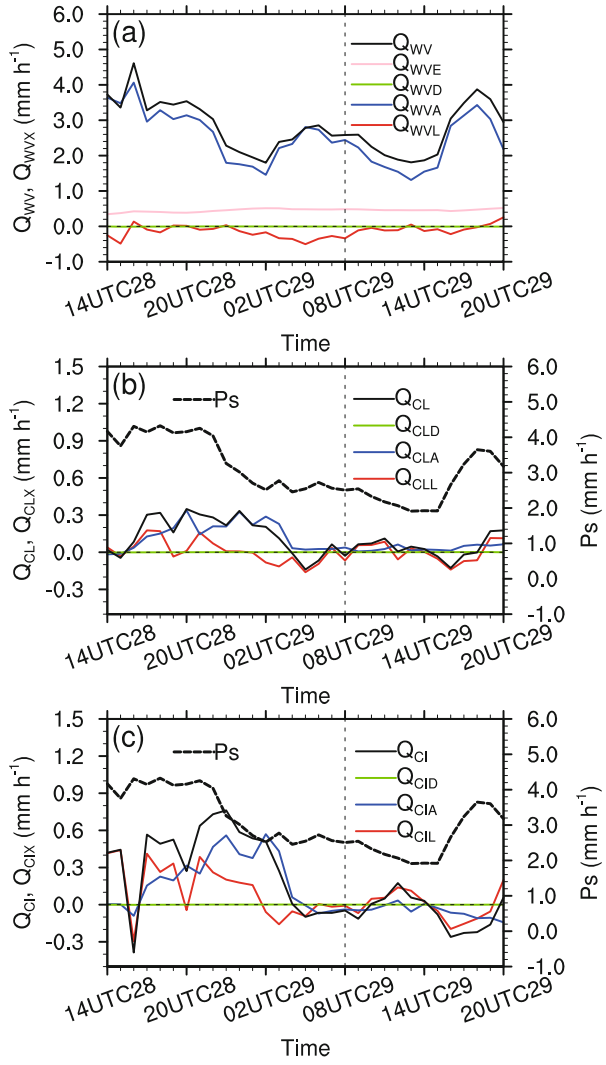

Fig. 4. Time series of area-averaged (a) moisture-related processes [Q_{WV} (black solid line), consisting of Q_{WVL} (red slid line), Q_{WVA} (blue solid line), Q_{WVD} (greed solid line), and Q_{WVE} (pink solid line)], (b) surface rain rate (P_S, black dash line) and liquid-phase cloud-related processes [Q_{CL} (black solid line), consisting of Q_{CLL} (red solid line), Q_{CLA} (blue solid line) and Q_{CLD} (green solid line)], and (c) surface rain rate (P_S, black dash line) and ice-phase cloud-related processes [Q_{CI} (black solid line), consisting of Q_{CIL} (red solid line), Q_{CIA} (blue solid line) and Q_{CID} (green solid line)] from 1400 UTC 28 June to 2000 UTC 29 June 2001 in a 240-km-radius domain. The vertical dashed line represents the genesis time of the TC and the horizontal dashed line represents "0". Units: mm h^{-1}.

again (negative Q_{CLL} and Q_{CIL}; Figs. 4b and c).

The 3D flux convergence/divergence term of hydrometeors [$\mathrm{ADV}_{Q_x} = -\nabla_3 \cdot (\rho_a Q_x \boldsymbol{V}), x \in (c, r, i, s, g)$ in Eqs. (3) and (4)] can be divided into the horizontal part [$-\nabla_h \cdot (\rho_a Q_x \boldsymbol{V})$, the vertical integration of which is denoted as Q_{CXA_H}] and the vertical part [$-\nabla_v \cdot (\rho_a Q_x \boldsymbol{V})$, the vertical integration of which is denoted as Q_{CXA_V}]. During the analysis period of this study, Q_{CXA_V} turned out to be much smaller than Q_{CXA_H} (not shown), indicating that the horizontal advection

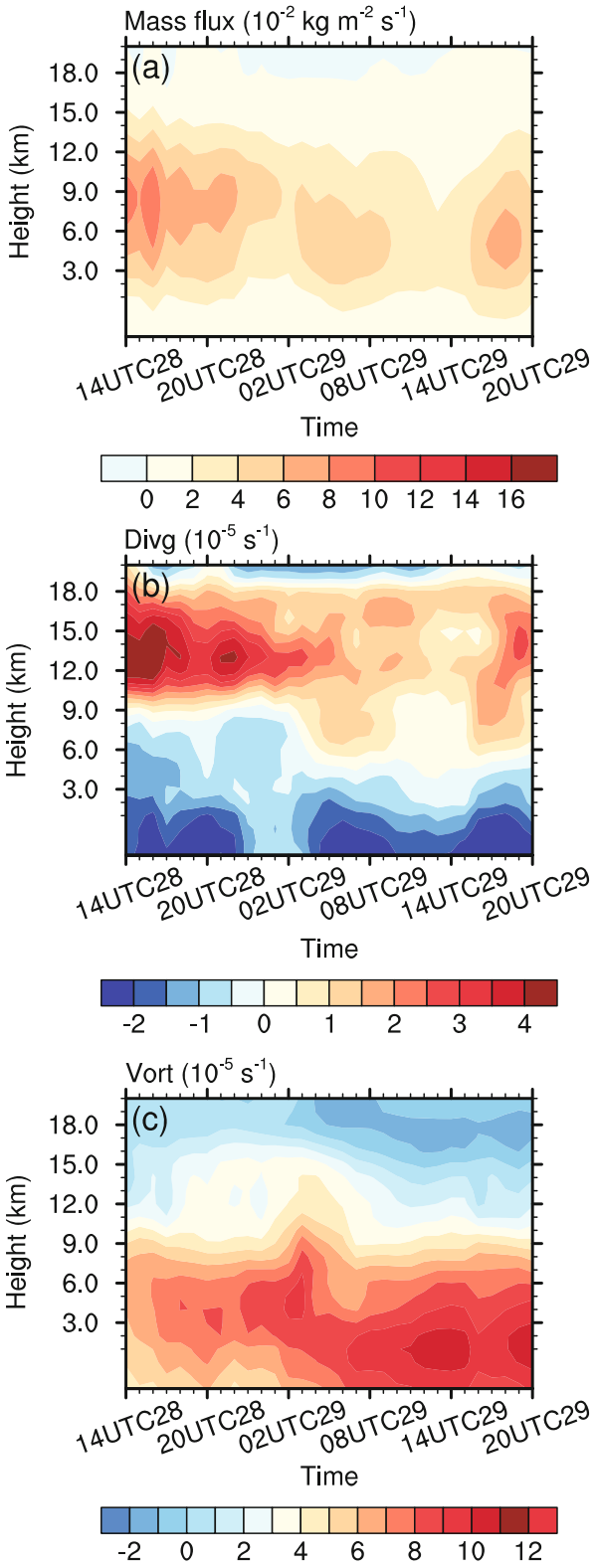

Fig. 5. Time series of area-averaged (a) vertical mass flux (units: 10^{-2} kg m^{-2} s^{-1}), (b) divergence (units: 10^{-5} s^{-1}), and (c) vertical relative vorticity (units: 10^{-5} s^{-1}) in a 240-km-radius domain.

of hydrometeors into or out of the 240 km-radius circular volume was more significant. Such a result is different from

the conclusions in Xu et al. (2017), stating that hydrometeor loss/convergence is related to the increased vertical advection of hydrometeors, while hydrometeor gain/divergence is associated with the decreased horizontal advection of hydrometeors. Liquid-phase hydrometeors (cloud water and rain water) were mainly distributed below $z = 6$ km (Figs. 6a and b). Induced by the low-level horizontal convergence below $z = 9$ km (Fig. 5b), the flux convergence of liquid-phase hydrometeors ($Q_{\mathrm{CLA\_H}} > 0$) occurred (Fig. 7). Before 0200 UTC 29 June, $Q_{\mathrm{CLA\_H}}$ generally increased. With the distinct decrease in rain water (Fig. 6b), as well as the apparent constriction of vertical convergence thickness and the decrease in upper-level divergence (Fig. 5b), $Q_{\mathrm{CLA\_H}}$ (Fig. 7) and Q_{CLA} (Fig. 4b) markedly decreased. Later, with the intensification of Durian, as well as the simultaneous enhancement of lower-tropospheric convergence and upper-level divergence (Fig. 5b), $Q_{\mathrm{CLA\_H}}$ (Fig. 7) and Q_{CLA} (Fig. 4b) increased again.

The ice-phase hydrometeors (cloud ice, snow and graupel) were mainly distributed above 4 km (Figs. 6c–e). Before 2000 UTC 28 June, negative $Q_{\mathrm{CIA\_H}}$ appeared above 9 km (Fig. 7) due to distinct upper-level divergence (Fig. 5b) and deep distributions of ice-phase hydrometeors (Figs. 6c–e). From 1800 UTC 28 to 0200 UTC 29 June, considerable positive $Q_{\mathrm{CIA\_H}}$ appeared between 4 km and 12 km (peaking between 6 km and 7 km), due to slightly enhanced lower-tropospheric convergence (Fig. 5b) and apparent distributions of snow and graupel (Figs. 6d and e). After 0200 UTC 29 June, with the distinct constriction of lower-tropospheric convergence thickness (Fig. 5b), the ice-phase hydrometeor convergence between 4 and 9 km at 0400 UTC 29 June converted to divergence above 4 km (Fig. 7). Meanwhile, due to the apparent decreases in ice-phase hydrometeors (Fig. 6), the magnitude of the above divergence above 4 km was relatively small (Fig. 7). Later, with the simultaneously enhancement of lower-tropospheric convergence and upper-level divergence (Fig. 5b) associated with the intensification of Durian, as well as the increases in ice-phase hydrometeors (Fig. 6), the magnitude of negative $Q_{\mathrm{CIA\_H}}$ increased slightly (Fig. 7).

The aforementioned analyses suggest that the precipitation during Durian's formation period was directly determined by the distribution of water species (water vapor and hydrometeors) and the environmental dynamics. At the same time, water species usually interact with each other in terms of microphysical conversion processes, which could exert crucial influence on the environmental thermodynamics and dynamics through latent heating or cooling. In the following section, the role played by microphysical latent heat in Durian's formation will be addressed.

4. Microphysical latent heat releases in Durian's formation

The temporal variations of the main domain-averaged and vertically integrated microphysical conversion rates associated with hydrometeors are shown in Fig. 8. The micro-

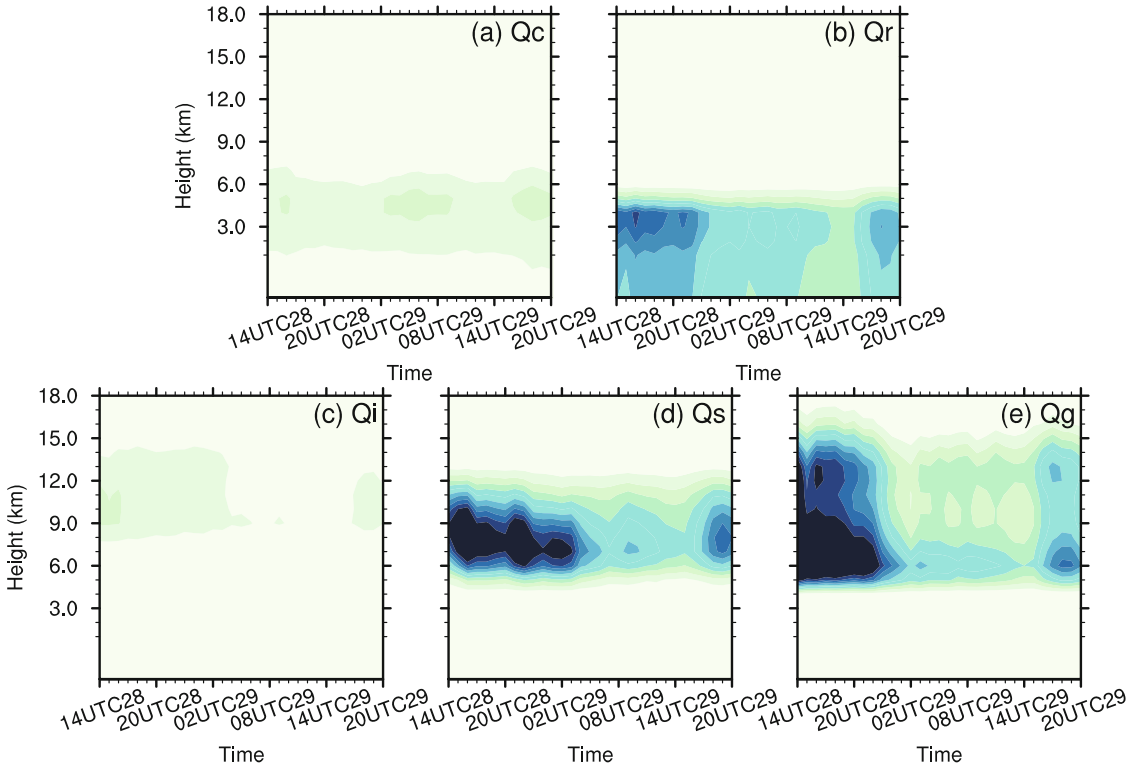

Fig. 6. Time–height cross sections of cloud hydrometeors: (a) cloud water (Qc), (b) rain water (Qr), (c) cloud ice (Qi), (d) snow (Qs) and (e) graupel (Qg), area-averaged in the 240-km-radius domain from 1400 UTC 28 June to 2000 UTC 29 June 2001. Units: 10^{-3} g g^{-1}.

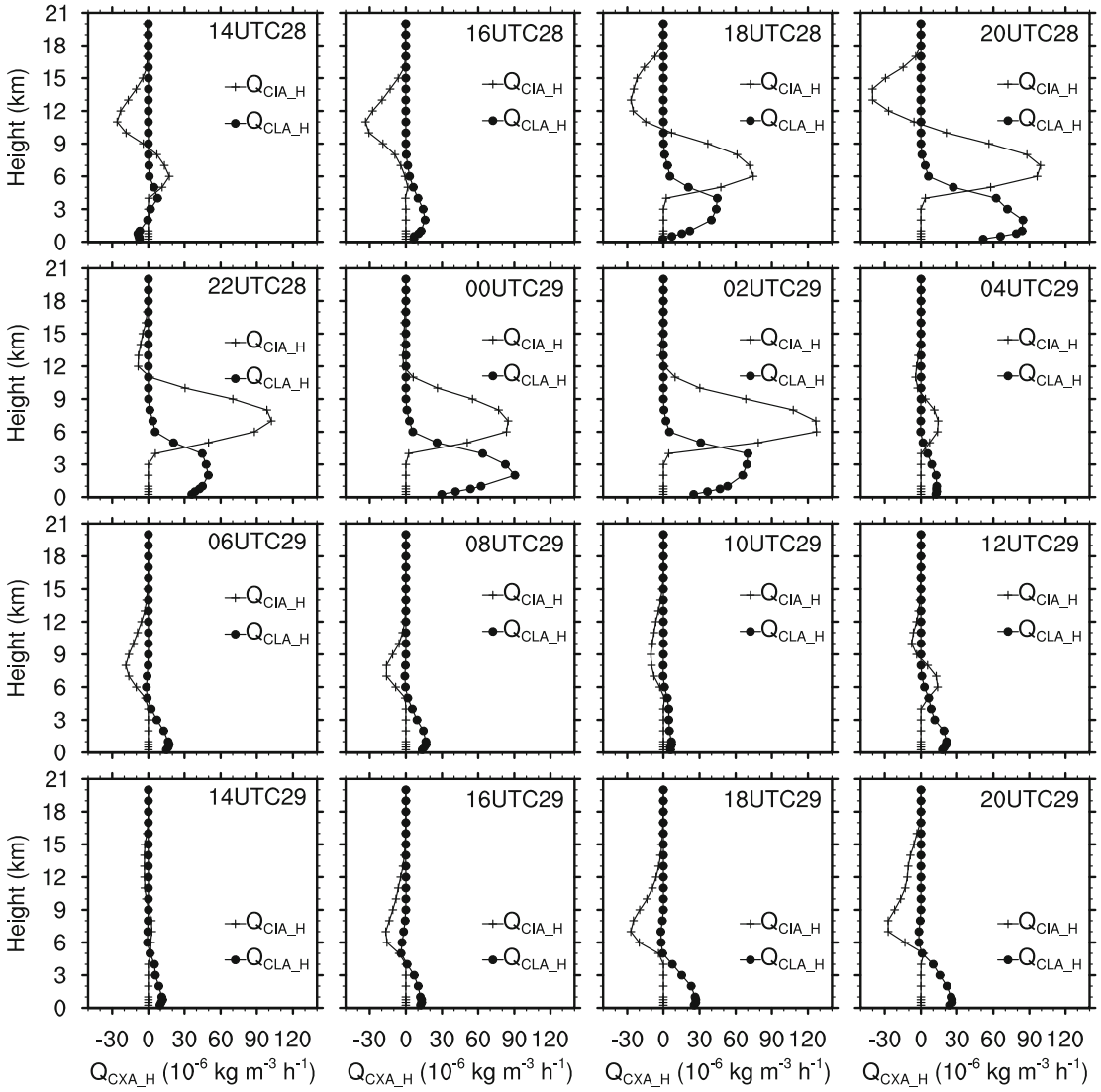

Fig. 7. Vertical profiles of area-averaged horizontal advection terms of liquid-phase hydrometeors ($Q_{\mathrm{CLA\_H}}$) and ice-phase hydrometeors ($Q_{\mathrm{CIA\_H}}$) in the 240-km-radius domain from 1400 UTC 28 June to 2000 UTC 29 June 2001. Units: 10^{-6} kg m^{-3} h^{-1}.

physical conversion processes are listed in Table 2. The sum of the main microphysical conversion rates presented distinct positive values during the analysis period, which is consistent with the variation of P_{S} (Fig. 3a). In the context of microphysical sources/sinks, rain water mainly came from the accretion of cloud water by rain water (P_{racw}) and the melting of graupel (P_{gmlt}), which was partially consumed by the evaporation of rain water (E_{rn}) (Fig. 8a) and largely consumed through surface rainfall (Fig. 3a). Cloud water mainly came from water vapor condensation (C_{nd}), which was almost totally offset by accretion processes between cloud water and rain water (P_{racw}) as well as cloud water and graupel (D_{gacw}) (Fig. 8b). Graupel mainly came from D_{gacw} and was largely consumed by P_{gmlt} (Fig. 8e). The microphysical conversion rates associated with cloud ice and snow were smaller than those of cloud water, rain water and graupel (Fig. 8). Cloud ice mainly came from the deposition of water vapor to cloud ice (D_{ep}) and was largely consumed through the accretion of cloud ice by snow (P_{saci}) (Fig. 8c). Snow mainly came from

Table 2. Cloud microphysical processes.

Term	Microphysical process description
E_{rn}	Evaporation of rain water
P_{gmlt}	Melting of graupel
P_{racw}	Accretion of cloud water by rain water
D_{gacw}	Accretion of cloud water by graupel
P_{saci}	Accretion of cloud ice by snow
D_{ep}	Deposition of water vapor to cloud ice
W_{gacs}	Accretion of snow by graupel
P_{smlt}	Melting of snow
P_{racs}	Accretion of snow by rain water

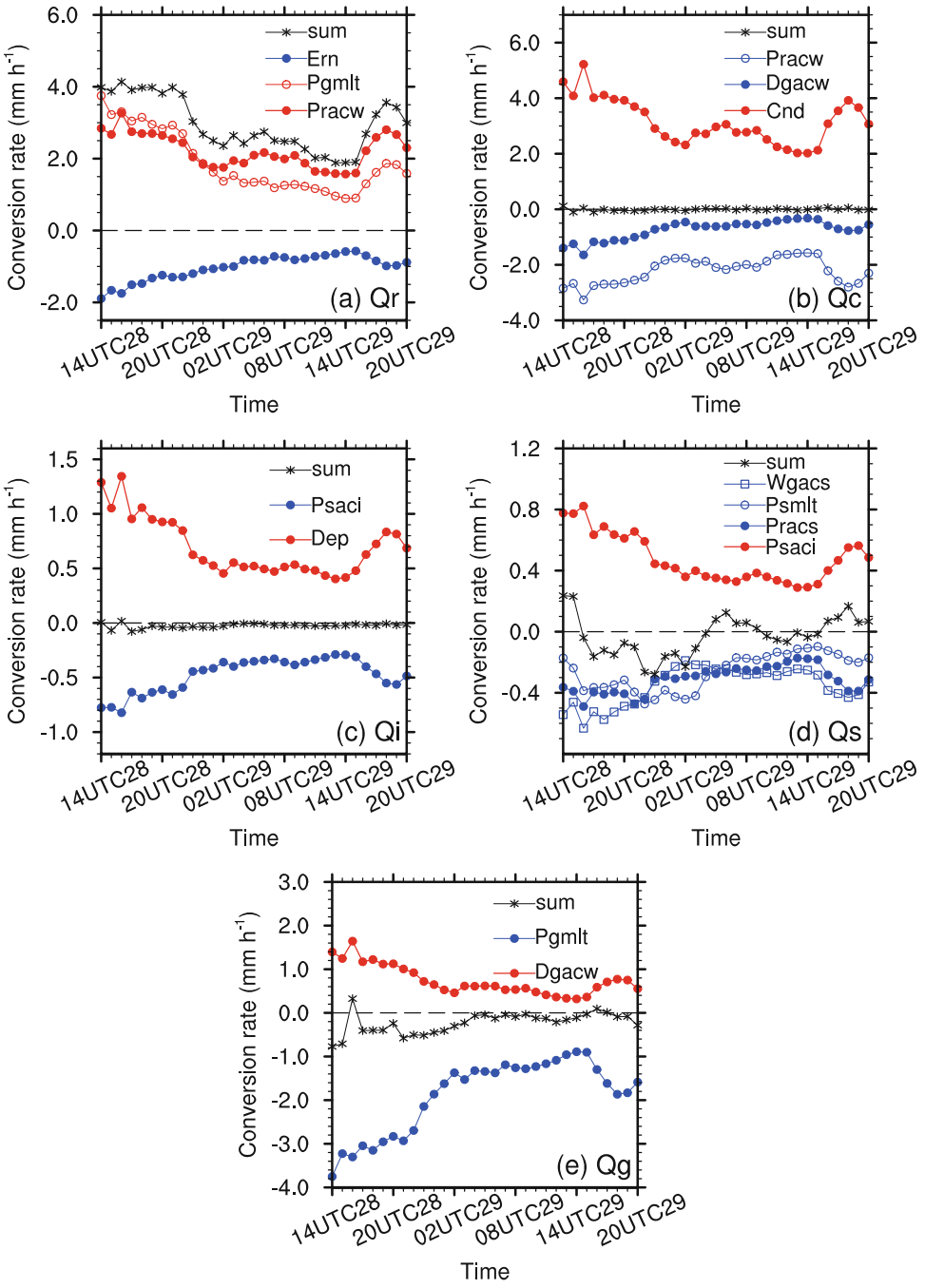

Fig. 8. Time series of the main vertically mass-integrated and area-averaged cloud microphysical conversion processes and the sum of all the conversion rates associated with (a) rain water, (b) cloud water, (c) ice, (d) snow and (e) graupel in the 240-km-radius domain from 1400 UTC 28 June to 2000 UTC 29 June 2001. E_{rn}: evaporation of rain; P_{gmlt}: melting of graupel; P_{racw}: accretion of cloud water by rain water; D_{gacw}: accretion of cloud water by graupel; C_{nd}: condensation of water vapor; P_{saci}: the accretion of cloud ice by snow; D_{ep}: deposition of water vapor; W_{gacs}: accretion of snow by graupel; P_{smlt}: melting of snow; P_{racs}: accretion of snow by rain water. Units: mm h^{-1}.

P_{saci}, and was mainly consumed by the accretion of snow by graupel (W_{gacs}), the melting of snow (P_{smlt}) and the accretion of snow by rain water (P_{racs}) (Fig. 8d). It is noted that the above microphysical conversion rates (Fig. 8) were largely influenced by the dynamical structures (Fig. 5).

On the other hand, the microphysical conversion processes not only contributed directly to the variations of hydrometeors but also indirectly impacted the thermodynamic environment of the atmosphere through latent heating/cooling (Fig. 9), and further exerted impact on the dynamical structure. The latent heating rate associated with condensation was the largest, mainly distributing below 9 km

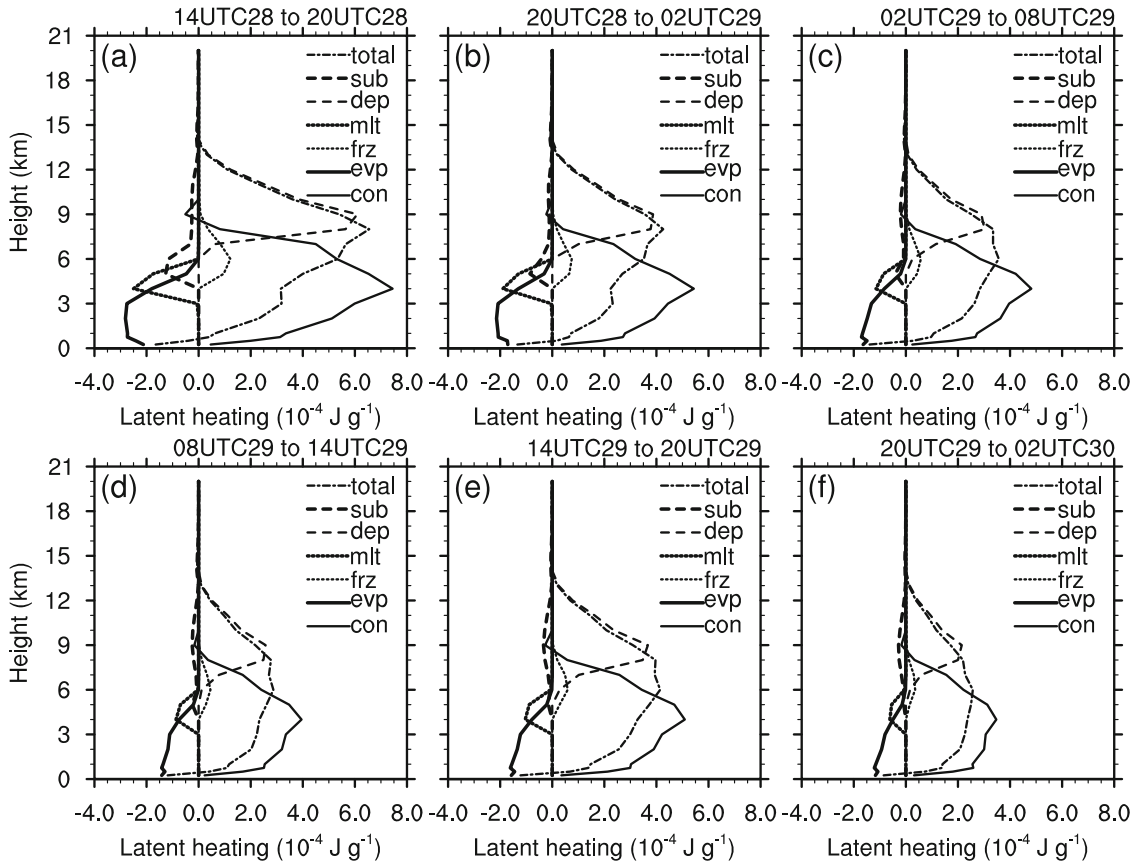

Fig. 9. Vertical profiles of temporally averaged and area-averaged latent heating/cooling rate associated with the sum of all cloud microphysical processes (total), condensation (con), evaporation (evp), freezing (frz), melting (mlt), deposition (dep) and sublimation (sub) processes in the 240-km-radius domain: (a) 1400 UTC to 2000 UTC 28 June; (b) 2000 UTC 28 to 0200 UTC 29 June; (c) 0200 UTC to 0800 UTC 29 June; (d) 0800 UTC to 1400 UTC 29 June; (e) 1400 UTC to 2000 UTC 29 June; (f) 2000 UTC 29 to 0200 UTC 30 June. Units: 10^{-4} J g^{-1}.

(Fig. 9). The narrow level of net cooling rate near the surface resulted from a very small condensation heating rate and distinct cooling rate by evaporation, which was mainly located beneath 6 km (Fig. 9). The latent heating rate associated with deposition processes, located from 6 km to 14 km, was the second largest heating rate (Fig. 9). This result echoes that in Cecelski and Zhang (2016)—that no tropical depression (TD)–scale disturbance occurs when removing the latent heat of fusion owing to depositional growth, emphasizing the effect of ice-phase microphysical processes in TC formation. The cooling rate by melting processes was the second largest cooling rate, located from 3 km to 6 km (Fig. 9). The latent heating/cooling rates associated with freezing and sublimation processes were relatively small. Cecelski and Zhang (2016) also found that removing homogeneous freezing has little impact on the development of the TD-scale disturbance. The magnitude of the net latent heating rate reduced (Figs. 9a–c) along with Durian's formation, and increased as Durian began to intensify (Figs. 9d and e), corresponding well with the variations of microphysical conversion rates (Fig. 8), dynamical structures (Figs. 5a and b) and rain rate (Fig. 3a). Before Durian's genesis (Figs. 9a and b), the maximum net latent heating rate was located at 8 km. Just before Durian's genesis (Fig. 9c), the height of the maximum net latent heating rate lowered distinctly to 6 km, mainly due to the more considerable decrease in the maximum deposition heating rate than the maximum condensation heating rate. Other heating/cooling rates, such as sublimation, evaporation and melting cooling rates, also played roles. The decrease and downward shift of the net latent heating peak mainly resulted from the deactivation of microphysical processes under the control of varied dynamical structure (Fig. 5). The changed vertical profile of net latent heating rate, on the contrary, could modify the thermal and dynamical structures of the atmosphere. Along with the downward shift of the net latent heating peak (Figs. 9 and 10) in this study, the "lower-tropospheric convergence superposed with upper-level divergence" dynamical structure (Fig. 5b) changed, accompanied by a more bottom-heavy vertical mass flux profile (Fig. 5a). Hence, mass and vorticity would be converged in a shallower layer (Fig. 5b), aiding the TC vortex spin-up in the lower troposphere (Raymond and Sessions, 2007; Raymond and López-Carrillo, 2011; Gjorgjievska and Raymond, 2014). While emphasizing the precipitation features from a microphysical perspective, we should not neglect the contribution of the precipitation processes to the dynamic

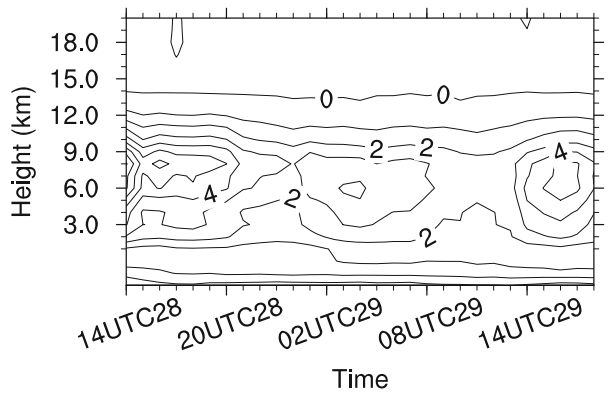

Fig. 10. Time–height cross section of area-averaged net latent heating (units: 10^{-4} J g^{-1}) in the 240-km-radius domain from 1400 UTC 28 June to 2000 UTC 29 June 2001.

and thermodynamic environment during TC formation. Wang et al. (2018a) compared the vorticity amplification among a set of sensitivity simulations of TC Durian (2001) with different convective and stratiform precipitation intensities. Results showed that inhibited precipitation, especially the inhibited convective precipitation, led to a weaker diabatic heating rate and upward mass flux, further retarding the near-surface vorticity convergence and amplification.

5. Summary and conclusions

In this study, the surface precipitation processes during the formation of TC Durian (2001) in the SCS were quantitatively investigated using the 3D WRF-based surface precipitation equation. The precipitation rate decreased slightly as the TC formation approached, and then increased again as the TC intensified. The water vapor–related processes ($Q_{\rm WV}$) contributed to about 80% of the surface precipitation during the genesis process, while the hydrometeor-related processes ($Q_{\rm CM}$) played a secondary role. After formation, the hydrometeor-related processes even made a negative contribution. The moisture-related processes were dominated by the 3D moisture advection term ($Q_{\rm WVA}$), and partly contributed by the surface evaporative process ($Q_{\rm WVE}$) as well. This result is basically consistent with the statements in Yang et al. (2011) and Braun (2006)—that moisture for precipitation is largely supplied by the horizontal water vapor convergence and partly originates from the ocean surface for TCs over the ocean. The sufficient moisture from $Q_{\rm WVA}$ and $Q_{\rm WVE}$ not only converted to precipitation eventually, but also moistened the local atmosphere before TC formation. As for the hydrometeor-related processes, the 3D cloud advection terms ($Q_{\rm CLA}$, $Q_{\rm CIA}$) and the local change terms ($Q_{\rm CLL}$, $Q_{\rm CIL}$) were the two dominant terms in both liquid-phase and ice-phase hydrometeor-related processes. Those terms largely decreased as the TC formed, and slightly reactivated as it intensified. After TC formation, terms $Q_{\rm CLL}$ and $Q_{\rm CIL}$ even made negative contributions to precipitation, indicating the development of TC cloud. However, in Xu et al. (2017), only the hydrometeor flux convergence/divergence term dominated the hydrometeor-related process. The variations of advection terms ($Q_{\rm WVA}$ and $Q_{\rm CLA}$, $Q_{\rm CIA}$) were largely determined by the vertical distributions of both the water vapor/cloud hydrometeors and the convergence/divergence configuration. As the TC formed, the lower-tropospheric convergence layer became shallower, while the upper-tropospheric divergence became weaker.

The effects of cloud microphysical conversion processes among different water species on the dynamic environment through latent heating/cooling were further diagnosed. The net latent heating center associated with the microphysical conversion processes became lower as the TC generated, as a result of less sublimation and more lower-tropospheric condensation. The downward shift of the latent heating center induced a more bottom-heavy upward mass flux profile, which was conducive to constraint of the lower-tropospheric convergence in a shallower layer and further helped the near-surface vortex spin-dup.

It should be noted that the above results are based on the water budget calculation of a single TC case from a numerical simulation using the WRF model. Although the water budget analysis method in this study is similar with those in some previous studies (Braun, 2006; Yang et al., 2011; Huang et al., 2014; Xu et al., 2017), the magnitude of the budget terms may be sensitive to the choice of microphysics scheme, the weather system and model configurations. Besides, many studies show that utilizing different microphysics schemes would result in significant changes in intensity and inner-core structure of TCs, as well as the associated clouds, precipitation, specific microphysical conversion processes and latent heating profiles (Wang, 2002; McFarquhar et al., 2006; Zhu and Zhang, 2006; Jin et al., 2014; Bao et al., 2016; Cecelski and Zhang, 2016). While McFarquhar et al. (2006) and Cecelski and Zhang (2016) emphasized the importance of ice-phase cloud parameterizations for TC simulations, we also find a nonnegligible role played by ice-phase hydrometeor processes in precipitation processes and in diabatic heating during TC formation. More studies about rainfall processes and the latent heating profiles associated with microphysical processes, especially the ice microphysics parameterization, during TC genesis are needed to generalize the results from this study.

Acknowledgements. Yaping WANG and Xiaopeng CUI are supported by the National Basic Research (973) Program of China (Grant No. 2015CB452804).

REFERENCES

Bao, J. W., S. A. Michelson, and E. D. Grell, 2016: Pathways to the production of precipitating hydrometeors and tropical cyclone development. *Mon. Wea. Rev.*, **144**, 2395–2420, https://doi.org/10.1175/MWR-D-15-0363.1.

Braun, S. A., 2006: High-resolution simulation of Hurricane Bonnie (1998). Part II: Water budget. *J. Atmos. Sci.*, **63**, 43–64,

https://doi.org/10.1175/JAS3609.1.

Cecelski, S. F., and D. L. Zhang, 2016: Genesis of Hurricane Julia (2010) within an African easterly wave: Sensitivity to ice microphysics. *Journal of Applied Meteorology and Climatology*, **55**, 79–92, https://doi.org/10.1175/JAMC-D-15-0105.1.

Chen, S. M., Y. K. Qian, and S. Q. Peng, 2015: Effects of various combinations of boundary layer schemes and microphysics schemes on the track forecasts of tropical cyclones over the South China Sea. *Natural Hazards*, **78**, 61–74, https://doi.org/10.1007/s11069-015-1697-7.

Cui, X. P., 2008: A cloud-resolving modeling study of diurnal variations of tropical convective and stratiform rainfall. *J. Geophys. Res*., **113**, D2, https://doi.org/10.1029/2007JD008990.

Cui, X. P., 2009: Quantitative diagnostic analysis of surface rainfall processes by surface rainfall equation. *Chinese Journal of Atmospheric Sciences*, **33**, 375–387, https://doi.org/10.3878/j.issn.1006-9895.2009.02.15. (in Chinese)

Cui, X. P., and X. F. Li, 2006: Role of surface evaporation in surface rainfall processes. *J. Geophys. Res*., **111**, D17, https://doi.org/10.1029/2005JD006876.

Cui, X. P., and X. F. Li, 2009: Diurnal responses of tropical convective and stratiform rainfall to diurnally varying sea surface temperature. *Meteor. Atmos. Phys*., **104**, 53–61, https://doi.org/10.1007/s00703-008-0016-1.

Cui, X. P., and F. W. Xu, 2009: A cloud-resolving modeling study of surface rainfall processes associated with landfalling typhoon Kaemi (2006). *Journal of Tropical Meteorology*, **15**, 181–191, https://doi.org/10.3969/j.issn.1006-8775.2009.02.007.

Cui, X. P., and X. F. Li, 2011: A cloud-resolving modeling study of short-term surface rainfall processes. *Meteor. Atmos. Phys*., **111**, 1–11, https://doi.org/10.1007/s00703-010-0121-9.

Cui, X. P., Y. Zhou, and X. F. Li, 2007: Cloud microphysical properties in tropical convective and stratiform regions. *Meteor. Atmos. Phys*., **98**, 1–11, https://doi.org/10.1007/s00703-006-0228-1.

Dunkerton, T. J., M. T. Montgomery, and Z. Wang, 2009: Tropical cyclogenesis in a tropical wave critical layer: Easterly waves. *Atmos. Chem. Phys.*, **9**, 5587–5646, https://doi.org/10.5194/acp-9-5587-2009.

Fritz, C., and Z. Wang, 2014: Water vapor budget in a developing tropical cyclone and its implication for tropical cyclone formation. *J. Atmos. Sci*., **71**, 4321–4332, https://doi.org/10.1175/JAS-D-13-0378.1.

Gao, S. T., and X. F. Li, 2010: Precipitation equations and their applications to the analysis of diurnal variation of tropical oceanic rainfall. *J. Geophys. Res*., **115**, https://doi.org/10.1029/2009JD012452.

Gao, S. T., X. P. Cui, Y. S. Zhou, and X. F. Li, 2005: Surface rainfall processes as simulated in a cloud-resolving model. *J. Geophys. Res*., **110**, https://doi.org/10.1029/2004JD005467.

Gao, S. T., X. P. Cui, and X. F. Li, 2009: A modeling study of diurnal rainfall variations during the 21-day period of TOGA COARE. *Adv. Atmos. Sci*., **26**(5), 895–905, https://doi.org/10.1007/s00376-009-8123-6.

Gjorgjievska, S., and D. J. Raymond, 2014: Interaction between dynamics and thermodynamics during tropical cyclogenesis. *Atmos. Chem. Phys.*, **14**, 3065–3082, https://doi.org/10.5194/acp-14-3065-2014.

Hong, S. Y., Y. Noh, and J. Dudhia, 2006: A new vertical diffusion package with an explicit treatment of entrainment processes. *Mon. Wea. Rev*., **134**, 2318–2341, https://doi.org/10.1175/MWR3199.1.

Huang, H. L., M. J. Yang, and C. H. Sui, 2014: Water budget and precipitation efficiency of Typhoon Morakot (2009). *J. Atmos. Sci*., **71**, 112–129, https://doi.org/10.1175/JAS-D-13-053.1.

Huang, Y. J., X. P. Cui, and X. F. Li, 2016: A three-dimensional WRF-based precipitation equation and its application in the analysis of roles of surface evaporation in a torrential rainfall event. *Atmos. Res.*, **169**, 54–64, https://doi.org/10.1016/j.atmosres.2015.09.026.

Jin, Y., and Coauthors, 2014: The impact of ice phase cloud parameterizations on tropical cyclone prediction. *Mon. Wea. Rev*., **142**, 606–625, https://doi.org/10.1175/MWR-D-13-00058.1.

Joyce, R. J., J. E. Janowiak, P. A. Arkin, and P. P. Xie, 2004: CMORPH: A method that produces global precipitation estimates from passive microwave and infrared data at high spatial and temporal resolution. *Journal of Hydrometeorology*, **5**, 487–503, https://doi.org/10.1175/1525-7541(2004)005<0487:CAMTPG>2.0.CO;2.

Kain, J. S., 2004: The Kain–Fritsch convective parameterization: An update. *J. Appl. Meteor*., **43**, 170–181, https://doi.org/10.1175/1520-0450(2004)043<0170:TKCPAU>2.0.CO;2.

Li, X., 2006: Cloud microphysical and precipitation responses to a large-scale forcing in the tropical deep convective regime. *Meteor. Atmos. Phys*., **94**, 87–102, https://doi.org/10.1007/s00703-005-0172-5.

Li, X. T., and S. F. Gao, 2016: *Cloud-Resolving Modeling of Convective Processes*. 2nd ed., Springer, 57–68.

Li, X. F., X. Y. Shen, and J. Liu, 2011: A partitioning analysis of tropical rainfall based on cloud budget. *Atmos. Res.*, **102**, 444–451, https://doi.org/10.1016/j.atmosres.2011.09.010.

Liao, F., Y. C. Hong, and G. G. Zheng, 2006: Research reviews of dynamic, thermodynamic and microphysical factors affecting cloud and precipitation. *Meteorological Monthly*, **32**, 3–11, https://doi.org/10.3969/j.issn.1000-0526.2006.11.001. (in Chinese with English abstract)

Liu, S. N., and X. P. Cui, 2018: Diagnostic analysis of rate and efficiency of torrential rainfall associated with Bilis (2006). *Chinese Journal of Atmospheric Sciences*, **42**, 192–208, https://doi.org/10.3878/j.issn.1006-9895.1704.17148. (in Chinese)

McFarquhar, G. M., H. N. Zhang, G. Heymsfield, J. B. Halverson, R. Hood, J. Dudhia, and F. Marks, 2006: Factors affecting the evolution of Hurricane Erin (2001) and the distributions of hydrometeors: Role of microphysical processes. *J. Atmos. Sci*., **63**, 127–150, https://doi.org/10.1175/JAS3590.1.

Montgomery, M. T., M. E. Nicholls, T. A. Cram, and A. B. Saunders, 2006: A vortical hot tower route to tropical cyclogenesis. *J. Atmos. Sci*., **63**, 355–386, https://doi.org/10.1175/JAS3604.1.

Pan, Y., J. J. Yu, J. Liao, and Y. Yu, 2011: Assessment on the rainfall monitoring of Typhoon Morakot by ground-gauged and satellite precipitation product. *Meteorological Monthly*, **37**, 564–570, https://doi.org/10.7519/j.issn.1000-0526.2011.5.007. (in Chinese)

Ping, F., Z. X. Luo, and X. F. Li, 2007: Microphysical and radiative effects of ice clouds on tropical equilibrium states: A two-dimensional cloud-resolving Modeling study. *Mon. Wea. Rev*., **135**, 2794–2802, https://doi.org/10.1175/MWR3419.1.

Ping, F., Z. X. Luo, and X. F. Li, 2008: Kinematics, cloud microphysics and spatial structures of tropical cloud clusters: A two-dimensional cloud-resolving modeling study. *Atmos. Res.*, **88**, 323–336, https://doi.org/10.1016/j.atmosres.2007.11.027.

Raymond, D. J., 2012: Balanced thermal structure of an intensifying tropical cyclone. *Tellus A*, **64**, 19181, https://doi.org/10.3402/tellusa.v64i0.19181.

Raymond, D. J., and S. L. Sessions, 2007: Evolution of convection during tropical cyclogenesis. *Geophys. Res. Lett*., **34**, L06811, https://doi.org/10.1029/2006GL028607.

Raymond, D. J., and C. López-Carrillo, 2011: The vorticity budget of developing typhoon Nuri (2008). *Atmos. Chem. Phys.*, **11**, 147–163, https://doi.org/10.5194/acp-11-147-2011.

Raymond, D. J., S. L. Sessions, and C. López-Carrillo, 2011: Thermodynamics of tropical cyclogenesis in the northwest Pacific. *J. Geophys. Res*, **116**, https://doi.org/10.1029/2011JD015624.

Sapiano, M. R. P., and P. A. Arkin, 2009: An intercomparison and validation of high-resolution satellite precipitation estimates with 3-hourly gauge data. *Journal of Hydrometeorology*, **10**, 149–166, https://doi.org/10.1175/2008JHM1052.1.

Shen, X. Y., Y. Wang, and X. F. Li, 2011a: Effects of vertical wind shear and cloud radiative processes on responses of rainfall to the large-scale forcing during pre-summer heavy rainfall over southern China. *Quart. J. Roy. Meteor. Soc*., **137**, 236–249, https://doi.org/10.1002/qj.735.

Shen, X. Y., Y. Wang, and X. F. Li, 2011b: Radiative effects of water clouds on rainfall responses to the large-scale forcing during pre-summer heavy rainfall over southern China. *Atmos. Res.*, **99**, 120–128, https://doi.org/10.1016/j.atmosres.2010.09.011.

Shen, X. Y., N. Zhang, and X. F. Li, 2011c: Effects of large-scale forcing and ice clouds on pre-summer heavy rainfall over southern China in June 2008: A partitioning analysis based on surface rainfall budget. *Atmos. Res.*, **101**, 155–163, https://doi.org/10.1016/j.atmosres.2011.02.001.

Skamarock, W. C., and Coauthors, 2008: A description of the advanced research WRF version 3. NCAR Technical Note NCAR/TN-475+STR, 113 pp, https://doi.org/10.5065/D68S4MVH.

Tao, W. K., J. Simpson, and M. McCumber, 1989: An ice-water saturation adjustment. *Mon. Wea. Rev*., **117**, 231–235, https://doi.org/10.1175/1520-0493(1989)117<0231:AIWSA>2.0.CO;2.

Wang, D. H., X. F. Li, W. K. Tao, Y. Liu, and H. G. Zhou, 2009: Torrential rainfall processes associated with a landfall of severe tropical storm Bilis (2006): A two-dimensional cloud-resolving modeling study. *Atmos. Res.*, **91**, 94–104, https://doi.org/10.1016/j.atmosres.2008.07.005.

Wang, D. H., X. F. Li, and W. K. Tao, 2010a: Torrential rainfall responses to radiative and microphysical processes of ice clouds during a landfall of severe tropical storm Bilis (2006). *Meteor. Atmos. Phys*., **109**, 107–114, https://doi.org/10.1007/s00703-010-0097-5.

Wang, J. J., X. F. Li, and L. D. Carey, 2007: Evolution, structure, cloud microphysical, and surface rainfall processes of monsoon convection during the South China Sea Monsoon Experiment. *J. Atmos. Sci*., **64**, 360–380, https://doi.org/10.1175/JAS3852.1.

Wang, X. H., X. P. Cui, and S. F. Hao, 2018b: Diagnostic and numerical study on surface rainfall processes of tropical cyclone Soudelor (2015) over sea. *Chinese Journal of Atmospheric Sciences*, https://doi.org/10.3878/j.issn.1006-9895.1804.18118. (in press, in Chinese)

Wang, Y. P., X. P. Cui, X. F. Li, W. L. Zhang, and Y. J. Huang, 2016a: Kinetic energy budget during the genesis period of tropical cyclone Durian (2001) in the South China Sea. *Mon. Wea. Rev*., **144**, 2831–2854, https://doi.org/10.1175/MWR-D-15-0042.1.

Wang, Y. P., X. P. Cui, and Y. J. Huang, 2016b: Characteristics of multiscale vortices in the simulated formation of Typhoon Durian (2001). *Atmospheric Science Letters*, **17**, 492–500. https://doi.org/10.1002/asl.683.

Wang, Y. P., Y. J. Huang, and X. P. Cui, 2018a: Impact of mid- and upper-level dry air on tropical cyclone genesis and intensification: A modeling study of Durian (2001). *Adv. Atmos. Sci*., **35**, 1505–1521, https://doi.org/10.1007/s00376-018-8039-0.

Wang, Y. Q., 2002: An explicit simulation of tropical cyclones with a triply nested movable mesh primitive equation model: TCM3. Part II: Model refinements and sensitivity to cloud microphysics parameterization. *Mon. Wea. Rev*., **130**, 3022–3036, https://doi.org/10.1175/1520-0493(2002)130<3022:AESOTC>2.0.CO;2.

Wang, Z., and I. Hankes, 2016: Moisture and precipitation evolution during tropical cyclone formation as revealed by the SSM/I–SSMIS retrievals. *J. Atmos. Sci*., **73**, 2773–2781, https://doi.org/10.1175/JAS-D-15-0306.1.

Wang, Z., M. T. Montgomery, and T. J. Dunkerton, 2010b: Genesis of pre-hurricane Felix (2007). Part II: Warm core formation, precipitation evolution, and predictability. *J. Atmos. Sci*., **67**, 1730–1744, https://doi.org/10.1175/2010JAS3435.1.

Xu, H. Y., G. Q. Zhai, and X. F. Li, 2017: Precipitation efficiency and water budget of Typhoon Fitow (2013): A particle trajectory study. *Journal of Hydrometeorology*, **18**, 2331–2354, https://doi.org/10.1175/JHM-D-16-0273.1.

Xu, X. F., F. W. Xu, and B. Li, 2007: A cloud-resolving modeling study of a torrential rainfall event over China. *J. Geophys. Res*., **112**, https://doi.org/10.1029/2006JD008275.

Yang, M. J., S. A. Braun, and D. S. Chen, 2011: Water budget of Typhoon Nari (2001). *Mon. Wea. Rev*., **139**, 3809–3828, https://doi.org/10.1175/MWR-D-10-05090.1.

Yu, Z. F., H. Yu, P. Y. Chen, C. H. Qian, and C. J. Yue, 2009: Verification of tropical cyclone–related satellite precipitation estimates in mainland China. *Journal of Applied Meteorology and Climatology*, **48**, 2227–2241, https://doi.org/10.1175/2009JAMC2143.1.

Yue, C. J., and S. W. Shou, 2011: Responses of precipitation to vertical wind shear, radiation, and ice clouds during the landfall of Typhoon Krosa (2007). *Atmos. Res.*, **99**, 344–352, https://doi.org/10.1016/j.atmosres.2010.11.003.

Yue, C. J., S. W. Shou, and X. F. Li, 2009: Water vapor, cloud, and surface rainfall budgets associated with the landfall of Typhoon Krosa (2007): A two-dimensional cloud-resolving modeling study. *Adv. Atmos. Sci*., **26**(6), 1198–1208, https://doi.org/10.1007/s00376-009-8135-2.

Zhang, W. L., X. P. Cui, A. S. Wang, and Z. P. Zong, 2008: Numerical simulation of hot towers during pre-genesis stage of Typhoon Durian (2001). *Journal of Tropical Meteorology*, **24**, 619–628, https://doi.org/10.3969/j.issn.1004-4965.2008.06.006. (in Chinese)

Zhu, T., and D.-L. Zhang, 2006: Numerical simulation of Hurricane Bonnie (1998). Part II: Sensitivity to varying cloud microphysical processes. *J. Atmos. Sci*., **63**, 109–126, https://doi.org/10.1175/JAS3599.1.